Article

Synthesis of Bi-Metallic-Sulphides/MOF-5@graphene Oxide Nanocomposites for the Removal of Hazardous Moxifloxacin

Aqsa Anum [1], Muhammad Altaf Nazir [1], Sobhy M. Ibrahim [2], Syed Shoaib Ahmad Shah [3], Asif A. Tahir [4], Misbah Malik [1], Muhammad Ahmad Wattoo [5] and Aziz ur Rehman [1],*

[1] Institute of Chemistry, The Islamia University of Bahawalpur, Bahawalpur 63100, Pakistan; anch39@gmail.com (M.A.N.)

[2] Department of Biochemistry, College of Science, King Saud University, P.O. Box 2455, Riyadh 11451, Saudi Arabia; syakout@ksu.edu.sa

[3] Department of Chemistry, School of Natural Sciences, National University of Sciences and Technology, Islamabad 44000, Pakistan

[4] Solar Energy Research Group, Environment and Sustainability Institute, Faculty of Environment Science and Economy, University of Exeter, Penryn Campus, Penryn TR10 9FE, UK

[5] Department of Chemistry, The Quaid i Azam University Islamabad, Islamabad 15320, Pakistan

* Correspondence: draziz@iub.edu.pk or azizypk@yahoo.com

Abstract: The development of new and advanced materials for various environmental and energy applications is a prerequisite for the future. In this research, the removal of hazardous moxifloxacin (MOX) is accomplished by synthesizing new hybrids of MOF-5 i.e., $Ni/Mo.S_2/MOF-5/GO$, $Ni.S_2/MOF-5/GO$, $Mo.S_2/MOF-5/GO$, and $Ni/Mo.S_2/MOF-5$ nanocomposites by using a metal-organic framework (MOF-5) and graphene oxide (GO) as a precursor. The introduction of $Ni_xMo_xS_2$ facilitates the unique interfacial charge transfer at the heterojunction, demonstrating a significant improvement in the separation effectiveness of the photochemical electron-hole pairs. To evaluate equilibrium adsorption capacity, time, pH, and concentration of organic pollutants were used as experimental parameters. The adsorption kinetics data reveals pseudo-first-order ($R^2 = 0.965$) kinetics when $Ni/Mo.S_2/MOF-5/GO$ photocatalyst was irradiated under light for 90 min against MOX degradation. This led to a narrow energy band gap (2.06 eV in $Ni/Mo.S_2/MOF-5/GO$, compared to 2.30 eV in $Ni/Mo.S_2/MOF-5$), as well as excellent photocatalytic activity in the photodegradation of moxifloxacin (MOX), listed in order: $Ni/Mo.S_2/MOF-5/GO$ (95%) > $Ni.S_2/MOF-5/GO$ (93%) > $Mo.S_2/MOF5/GO$ (90%) > $Ni/Mo.S_2/MOF-5$ (86%) in concentrations up to 2.0 mgL^{-1}, caused by the production of superoxide ($O_2^{\bullet-}$) and hydroxide ($OH^{\bullet}$) radicals, which encouraged the effective photocatalytic activities of the heterostructure. After five successive tests demonstrating its excellent mechanical stability, the impressive recyclability results for the $Ni/Mo.S_2/MOF-5/GO$ revealed only a tiny variation in efficiency from 95% (for the first three runs) to 93% (in the fourth run) and 90% (in the fifth run). These findings show that the heterostructure of $Ni/Mo.S_2/MOF-5/GO$ is an effective heterojunction photocatalyst for the quick elimination of moxifloxacin (MOX) from aqueous media.

Keywords: MOF; graphene; heterojunction; transition metals compounds; degradation; fluoroquinolones (FQs); moxifloxacin (MOX)

1. Introduction

A family of synthetic antibacterial substances known as fluoroquinolones (FQs) is becoming popular for majority of the nations in Europe and is one of the most typical antibiotics found in the treatment of wastewater [1]. In the animal agricultural industry, tetracycline, as well as enrofloxacin are widely used antibiotics for both treatment of infectious diseases in livestock animals and promotion of livestock growth, however, they are

also responsible for severe contamination of water bodies and soil [2]. Quinolones, especially second and third generation drugs, are used more frequently in human medicine [3]. A fluoroquinolone of the third generation, moxifloxacin (MOX), is commonly used to treat certain bacterial infections in humans and animals [4]. MOX's propensity for genotoxicity [5] makes its release and buildup in the environment a significant risk to ecosystems and health. Thus, a method for decontaminating the FQ drug moxifloxacin (MOX) from wastewater that is both efficient and affordable needs to be developed. Various techniques in practice for the exclusion of antibiotics and other noxious pollutants from water include adsorption, photo-Fenton, photo-degradation, and advanced oxidation processes [6–9]. Environmental remediation can be accomplished using sunlight-irradiated photo-degradation and is considered the most economic, most efficient, and productive technique for the treatment of waste water using various materials such as GO-based composites, hexaferrites, porous silica-based composites, metal oxide-based catalysts etc. [10–13].

Among all the promising classes of advanced materials, metal-organic frameworks (MOFs) are well-structured crystalline coordination polymers with large surface areas, exceptional absorbability, and strong catalytic properties [14–16]. Moreover, the crystallite sizes, chemical compositions, atomic weights, and weight percentages of the resultant nanocomposites and the optimized crystal phases can be easily controlled by controlling the conditions, such as the temperature, dwell time, heating rate and gaseous atmosphere etc. MOFs have been extensively applied in a variety of applications such as catalysis, energy-storage, supercapacitors, oxidation reduction reactions, and the adsorption of contaminants from polluted water [17–21].

MOF-5, first published in 1999, is composed of ZnO_4 units linked together by a 1,4-benzenedicarboxylate linker to form an extraordinary cubic lattice. The MOF-5, initially appearing as a cubic structure, came into prominence in 2002 [22]. As a result of using pristine MOFs containing heteroatoms or MOFs with metal/non-metal guests as precursors, it has been demonstrated that nanocomposites resulting from this procedure can be doped in situ with metals and/or heteroatoms such as N, C, S, and P to alter the semiconductor's electronic structure, semi-conductive properties, and energy band positions in order to improve solar absorption and charge separation. A number of factors prevent pristine MOFs from being a good candidate for direct photocatalytic applications, including the weak coordination bonds between metal ions (oxo-clusters) and organic linkers, the wide band gaps, and poor semi-conductive properties (limited charge generation and transfer). It has been reported that MOFs need to be coupled with other substances for adsorption, such as meso-porous SiO_2/(MOF), meso-porous Al_2O_3/(MOF), MOF/g-C_3N_4, and MOF/graphene [23] To enhance the photocatalytic performance of MOF derived nanocomposites, it is imperative to optimize the morphologies, compositions, electrical conductivity, and interfacial contacts [24–26]. GO, known to exist for about 150 years, is a carbon-based compound with many hydroxyl, epoxide, and carboxyl surface groups. By subjecting graphite to intense oxidizers, it is possible to produce graphene oxide (GO), which is composed of elements C, O, and H in varying proportions [13,27,28]. The concept of MOF-GO nanocomposites is based on specifications for the hydroxyl (OH) and epoxy functional groups of GO, which enable metal ions in MOFs to operate as composites. Therefore, GO can form nonporous, dense arrays of layers by fusing the complementary properties of two materials. Hydrothermal synthesis is a simple approach for synthesizing and increasing the mesoscopic regularity of a material by using a chemical process at low temperature and pressure. This study used a one-step hydrothermal technique to generate a hybrid of MOF-5 and GO. Recently, several novel findings on MOF-GO hybrids [29] have been reported employing a variety of MOFs, such as MOFs based on zinc (MOF-5) [30], zirconium MOF (UiO-66) [31], and iron (MIL-100) [32]. However, there is presently little study on the capacity of MOF-GO composites or their photocatalytic performance in the removal of noxious pollutants from waste water.

Molybdenum disulfide ($Mo.S_2$) exhibits a six-party condensed structure that is similar to graphene and exhibits good optical and electrical transmission properties. In particular,

Mo.S_2 nanosheets can enhance the number of reaction sites and are utilized as a non-noble metal catalyst to increase photocatalytic yield [33]. Metal ions of molybdenum and nickel can improve the structure of ligands and MOFs, which ultimately regulates the photocatalytic activity of MOF compounds. In the present work, the fabrication of MOF-5/GO using Ni.S_2 nanospheres was carried out via a solvothermal technique with Mo.S_2 coated on the surface of Ni.S_2 nanospheres, as outlined in the synthesis scheme. The high attraction created by homologous inorganic molecules between the nucleation sites was utilized in the construction of the Ni.S_2/Mo.S_2/MOF-5/GO nanocomposite.

This study focused on the development of an effective and efficient MOF-5/GO heterojunction for photocatalytic degradation of toxic antibiotics from simulated wastewaters. For this, the fabrication of MOF-5/GO was carried out to produce a series of nanocomposites: Ni/Mo.S_2/MOF-5/GO, Ni.S_2/MOF-5/GO, Mo.S_2/MOF-5/GO, and Ni/Mo.S_2/MOF-5. It is expected that the newly synthesized nanocomposites would expand the surface area and boost the amount of photogenerated electron-hole pairs, hence improving the photocatalytic activity of MOF-5/GO hybrids as they are formed. Photodegradation of pollutants, formation of reactive species such as superoxide and hydroxyl radicals, and formation of holes are the steps that lead to the transformation of organic pollutants into H_2O and CO_2. In our research, several factors are evaluated to determine how well the photodegradation process works [34], including the wavelength (UV, UV-Vis), intensity of incident light, pH value of the medium in the reactor, concentration of the photocatalysts and the organic pollutants, reaction time, and dynamics of charge carriers. We hope that researchers will be motivated by this work to investigate and develop new photocatalysts for the purification of water containing MOX and other noxious pollutants.

2. Results and Discussion

2.1. XRD Analysis

XRD patterns of Ni.S_x/Mo.S_x/MOF-5/GO are shown in Figure 1a–d while the MOF-5 is represented as (♣) in spectras. These graphs confirm the successful synthesis of nanocomposites Pristine MOF-5(♣) displays crystalline peaks at 2θ values 6.80°, 9.64°, 13.55°, 15.29°, 20.60°, 22.41°, 24.69°, 31.30°, and 32.12° for crystal planes 200, 220, 400, 420, 531, 533, 551, and 911 respectively [35].As seen in Figure 1a, GO has a distinctive, strong peak at 2θ = 26.5° that is attributed to 002. The MOF-5/GO exhibits diffraction peaks at 2θ = 10.12°, 15.61°, 18.55°, 20.58°, 25.95°, 27.27°, 28.39°, 30.31°, 31.12°, 32.34°, 34.06°, and 43.80° [36]. These peaks are somewhat displaced, but they do not alter the crystalline structure of the material. From the Ni/Mo.S_2/MOF-5, Ni.S_2/MOF-5/GO, and Ni-Mo.S_2/MOF-5/GO catalysts, peaks attributed to Ni.S_2 can be found at 2θ = 32.0° (200) and 45.6° (220), while Mo.S_2 presence was confirmed (PDF#75-1539) with indexes at 2θ = 35.25° (103) and 54.5° (106). The spectra also comprised a few peaks of Ni from NiS_2 at 62.2° and 75.01°, with indexes (220) and (311) along with peaks of Mo from Mo.S_2 at 49.32° and 71.71° which correspond to (200) and (101), respectively. Furthermore, different structural parameters of the prepared nanocomposites determined from XRD analysis are presented in Table 1.

Table 1. Geometric parameters of Ni/Mo.S_2/MOF-5/GO, Ni.S_2/MOF-5/GO, Mo.S_2/MOF-5/GO, Ni/Mo.S_2/MOF-5 nanocomposite determined from XRD analysis.

Nanocomposites	a (A°)	c (A°)	Volume (A°)³	Crystallite Size (nm)	Strain ε (Nm⁻²)	Dislocation Density (m⁻²)	Lattice Spacing (A°)
Ni/Mo.S_2/MOF-5/GO	3.561	5.6732	51.7324	24.0866	1.524×10^{-6}	1.760×10^{-6}	3.78
Ni.S_2/MOF-5/GO	2.4438	4.6071	24.6437	25.2436	1.495×10^{-6}	1.569×10^{-6}	2.47
Mo.S_2/MOF-5/GO	2.217	4.476	18.867	25.8973	1.456×10^{-6}	1.479×10^{-6}	2.59
Ni/Mo.S_2/MOF-5	3.1355	5.4291	46.9241	24.115	1.478×10^{-6}	1.659×10^{-6}	3.42
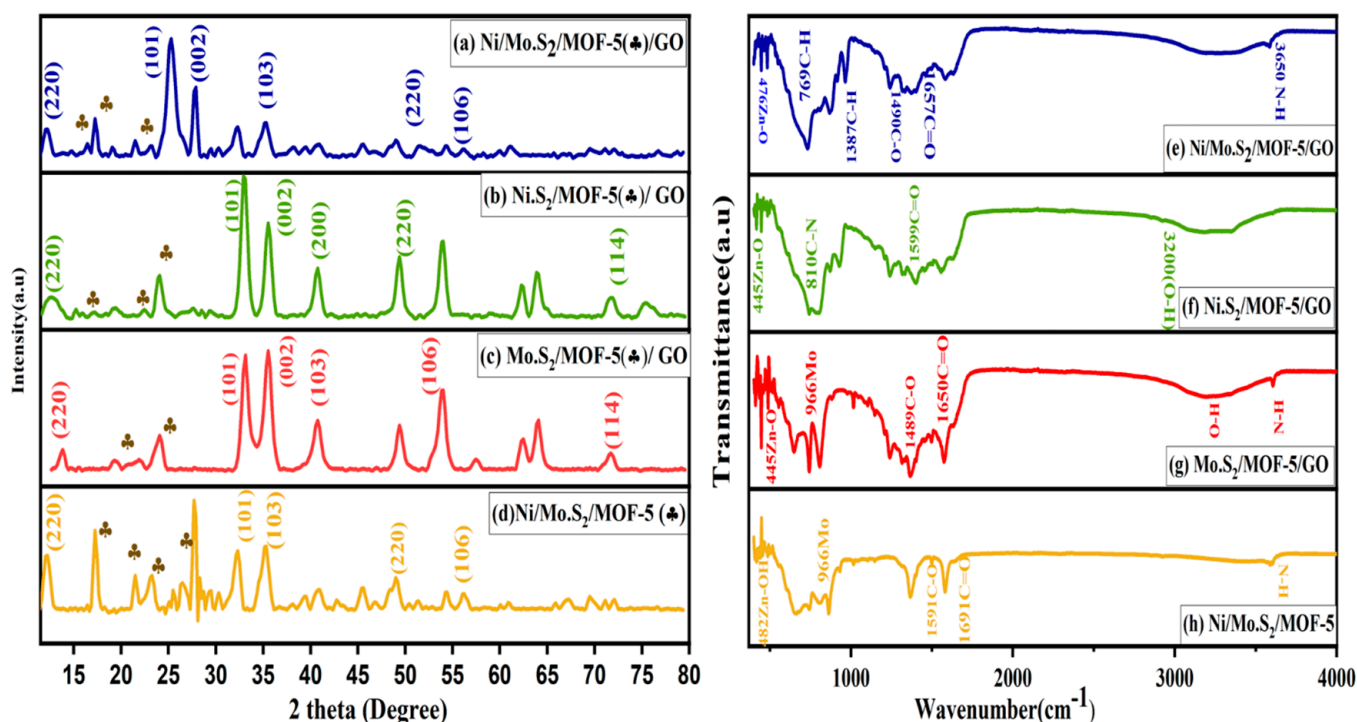
Figure 1. The XRD spectra of (**a**) Ni/Mo.S$_2$/MOF-5(♣)/GO, (**b**) Ni.S$_2$/MOF-5(♣)/GO, (**c**) Mo.S$_2$/MOF-5(♣)/GO, and (**d**) Ni/Mo.S$_2$/MOF-5(♣) and Fourier transform infrared (FTIR) spectra of sample (**e**) Ni/Mo.S$_2$/MOF-5/GO, (**f**) Ni.S$_2$/MOF-5/GO, (**g**) Mo.S$_2$/MOF-5/GO, (**h**) Ni/Mo.S$_2$/MOF-5 nanocomposites.

2.2. FTIR Analysis

The FTIR graphs of synthesized nanocomposites are depicted in Figure 1e–h. FTIR spectra of Ni/Mo.S$_2$/MOF-5/GO show significant distinctive bands of GO at 3416, 1657, 1490, 1218, 1040, and 860 cm^{-1} [37]. The typical peaks in GO include the stretching vibrations of the OH at 3416 cm^{-1}, C-O at 1490 cm^{-1} (carbonyl or carboxylic group), C=O at 1657 cm^{-1} (aromatic stretching frequency), and C-O at 1218 cm^{-1} (epoxy). The epoxy or peroxide functional group showed an absorption band at 860 cm^{-1}, while the C-O that belongs to alkoxy shows a stretching vibration band at 1040 cm^{-1}.

The MOF-5 shows two distinct bands at 1691 and 1599 cm^{-1} attributed to C=O and C-O stretching vibrations of the aromatic ring of terephthalic acid. However, distinctive peaks attributed to the aromatic ring of terephthalic acid in MOF-5 were observed in the vicinity of 1200–600 cm^{-1}. The band that appeared at 769 cm^{-1} corresponds to C-H stretching vibrations. The inset Figure 1e shows an absorption band at 476 cm^{-1} attributed to the Zn-O stretching [38]. The FTIR spectra of MOF-5/GO nanocomposites [39] show that GO [40] had no prominent effect on MOF-5 properties. Meanwhile, the peak at 2850 cm^{-1} demonstrates the existence of uncondensed NH$_3$. A few wide peaks at 3200 and 3650 cm^{-1} are due to OH and NH bonds, as displayed in Figure 1e,f, and another band at 2920 cm^{-1} is linked to adsorbed water molecules.

2.3. Morphology and Structure Analysis

The morphology of the synthesized nanocomposite materials was examined through SEM analysis. The SEM pictures in Figure 2a demonstrate that GO is incorporated into the MOF-5 framework without significantly changing its shape. Images taken by scanning electron microscope showed that the breakdown of the nanocomposite made from MOF-5 enabled the creation of flaky carbon nanostructures with graphene oxide acting as their support. Due to the presence of Na$_2$S in the synthesis of molybdenum disulfide, which generated a few irregular nanoparticles, the altered morphology of GO/MOF-5 indicated

the adherence of the metallic sulphides $Mo.S_2$ and Ni on the surface of GO/MOF-5. However, the $Ni/Mo.S_2$-modified MOF-5/GO has changed the shape of the tiny ball structure into a flaky structure, as seen in Figure 2b; thus, $Ni/Mo.S_2/MOF-5/GO$ was successfully developed. Additionally, EDS was performed to reveal the elemental composition of newly synthesized nanocomposites derived from MOF-5/GO. Nanocomposites provided valid evidence for elements like C, O, N, Cl, Zn, Ni, and Mo.
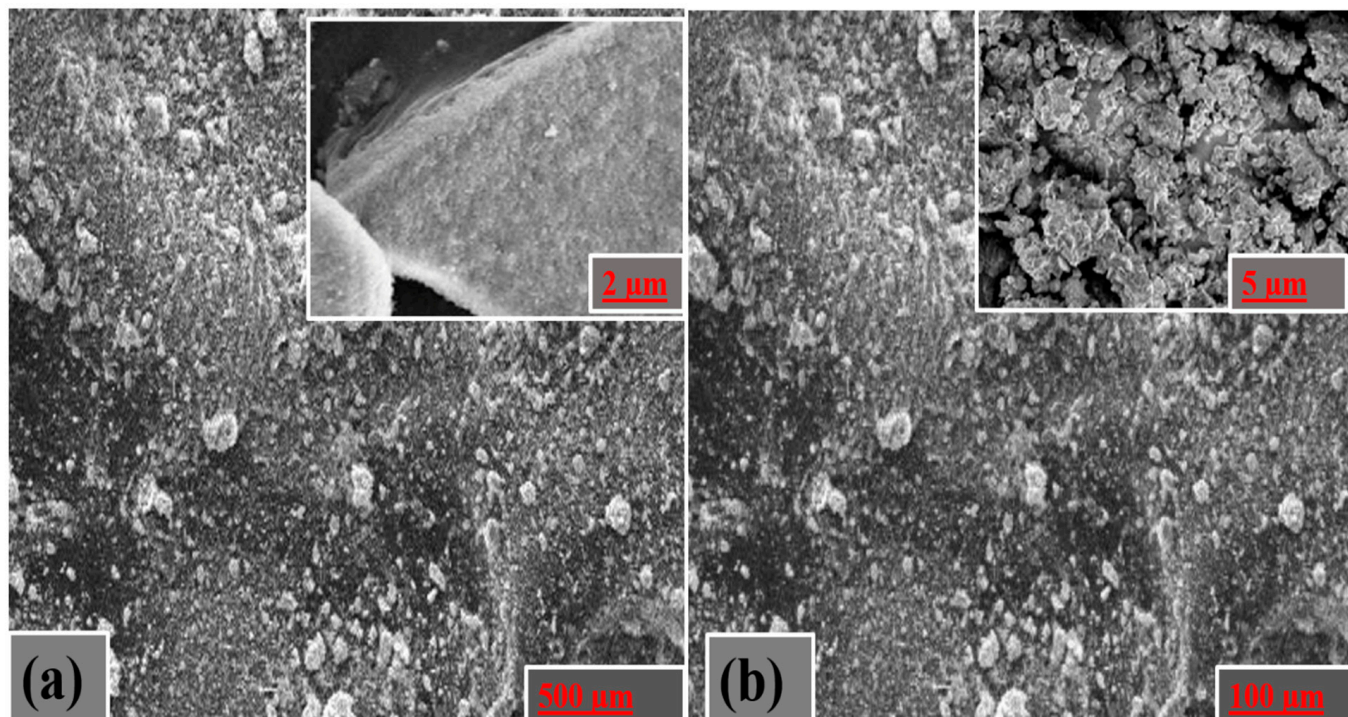
**Figure 2.** SEM images of (**a**) MOF-5/GO (**b**) $Ni/Mo.S_2/MOF-5/GO$.

2.4. Band Gap Turning Analysis

Using UV-visible spectroscopy, the band gap energies and absorbance spectra of the newly synthesized photocatalysts namely, $Ni/Mo.S_2/MOF-5/GO$, $Ni.S_2/MOF-5/GO$, $Mo.S_2/MOF-5/GO$, and $Ni/Mo.S_2/MOF-5$ were analyzed, as shown in Figure 3a. Their Tauc plots, as presented in Figure 3b, were drawn using the standard approach, and the following equation was used to determine the corresponding energies of these absorption peaks [41].

$$Eg = hc/\lambda_{absorption}. \tag{1}$$

where, Eg = optical band gap, c = velocity of light, h = Planck constant, and λ = wavelength.

The proposed photocatalytic nanocomposite $Ni/Mo.S_2/MOF-5/GO$ is a heterojunction between MOF-5/GO and bi-metallic sulphides ($Ni.S_2$, $Mo.S_2$). There was a significant increase in absorption due to the reduction in the energy band gap, from 2.30 eV to 2.06 eV, shown by $Ni-Mo.S_2/MOF-5$. The highest light absorption is demonstrated by $Ni/Mo.S_2/MOF-5/GO$, which leads to the highest photocatalytic activity. Moreover, enrichment in light absorption intensity also showed a viable increase in the number of photo-induced (e^-/h^+) pairs [42,43]. As a result, more active species are detected as ($O_2^{\bullet -}$) and ($OH^\bullet$) radicals. This ultimately led to enhanced photocatalytic activity of $Ni/Mo.S_2/MOF-5/GO$ [44].
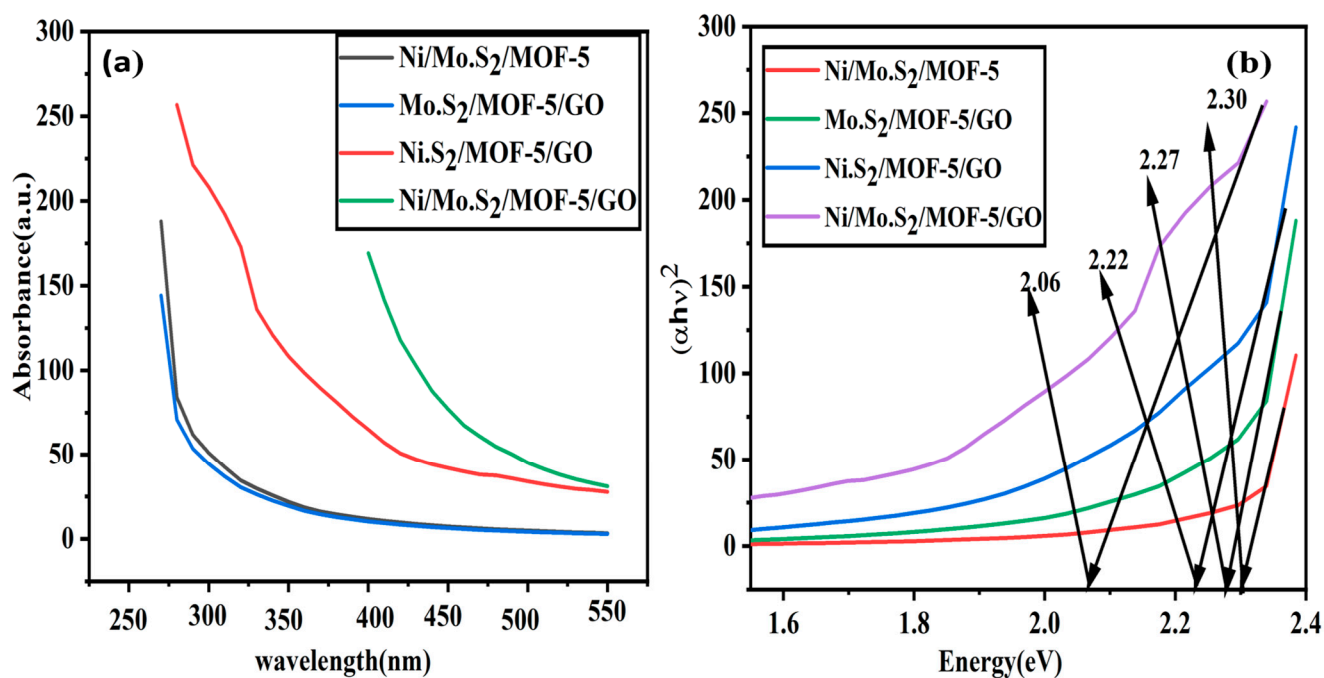
**Figure 3.** (**a**) Absorbance spectra and (**b**) Tauc's plot of Ni/Mo.S$_2$/MOF-5/GO, Ni.S$_2$/MOF-5/GO, Mo.S$_2$/MOF-5/GO, Ni/Mo.S$_2$/MOF-5 nanocomposites.

2.5. Photocatalytic Activity of MOF/GO

The well-known fluoroquinolone antibiotic, moxifloxacin was picked as a representative emerging hazard to study how effectively the synthesized materials function as photocatalysts when exposed to visible light. The MOX absorption spectra exhibit maximum absorption at approximately 288–300 nm in the presence of various photocatalysts when exposed to unfiltered sunlight, and it was observed that the MOX peak steadily reduced with time in the presence of all catalysts. In order to examine the effectiveness of the photocatalysis of nanocomposites composed of Ni/Mo.S$_2$/MOF-5/GO, Ni.S$_2$/MOF-5/GO, Mo.S$_2$/MOF-5/GO, and Ni/Mo.S$_2$/MOF-5 under sunlight illumination for 90 min, moxifloxacin (MOX) was subjected to photocatalytic degradation. As illustrated in Figure 4a–d, Ni/Mo.S$_2$/MOF-5/GO demonstrated 95% degradation efficiency, which, when compared to the other composite materials, indicates a narrower charge zone results in the formation of the best possible heterojunction, since all the composites that were synthesized were determined to be photocatalytically active for moxifloxacin (MOX). Electron hole recombination can be prevented by graphene's ability to operate as an electron receiver, taking in photoexcited electrons from semiconductors [45,46]. The absorption of visible light cannot be increased by graphene [47]. Visible light-absorbing graphene is required as a co-catalyst for MOF [48–50].

The influence of Ni.S$_x$/Mo.S$_x$/MOF-5/GO catalyst dosage, MOX concentration, and pH on MOX degradation by all catalysts as a function of time under sunlight irradiation was also checked; results are summarized in the supporting file as (Figure S1).
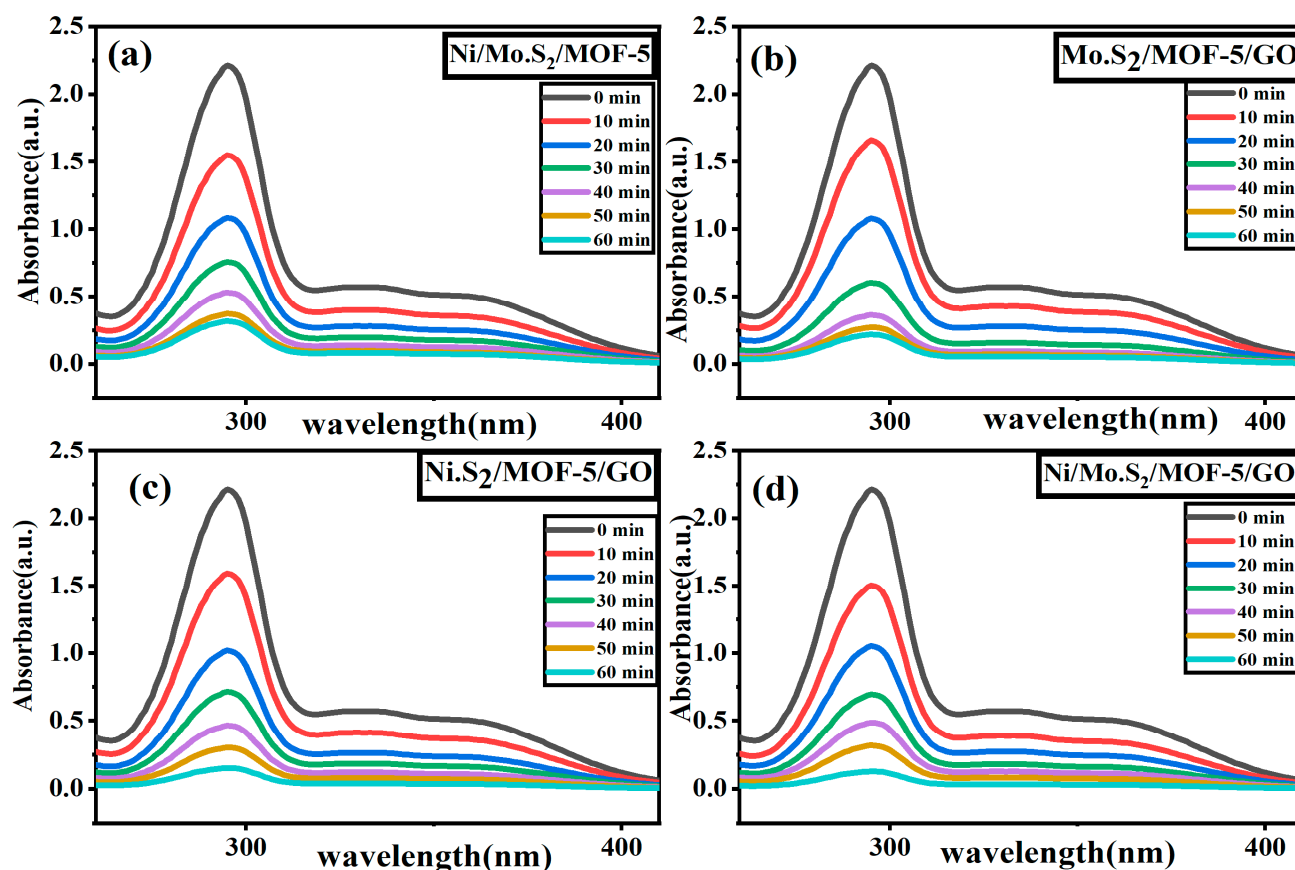
Figure 4. Absorbance spectra of moxifloxacin (MOX) (**a**) Ni/Mo.S$_2$/MOF-5/GO, (**b**) Mo.S$_2$/MOF-5/GO (**c**) Ni.S$_2$/MOF-5/GO, (**d**) Ni/Mo.S$_2$/MOF-5 nanocomposites.

2.6. Kinetics Studies of the Photodegradation of MOX

The increase in photocatalyst surface active sites, which in turn leads to an increase in the generation of species responsible for MOX photodegradation, including (e^-/h^+), ($O_2^{\bullet-}$), and ($OH^\bullet$), is the reason for accelerated degradation [51]. Although the additional catalyst causes the particles to assemble, which inhibits light from interacting with the catalyst and leads to the successive absorption of photons by the photocatalyst surface, the percentage degradation starts to decline above the optimal catalyst loading limit for each catalyst, and ultimately dampens the performance.

As a result, the activity of degradation is increased, and electron-hole pair recombination is decreased. The quantitatively given photodegradation reaction kinetics were studied using the linear fit model and were calculated by the following equations:

$$C_t = C_0 \, e^{-kt} \tag{2}$$

and

$$-\ln (C_t / C_0) = kt \tag{3}$$

where C_t = concentration at time t, C_0 = initial concentration, e = base e, k = rate constant of decline/day, t = time, and ln = natural log. By plotting $-\ln (C_t/C_0)$ on the y-axis and irradiation time (t) on the x-axis, a straight line is obtained, as shown in Figure 5a, where the k values of samples Ni/Mo.S$_2$/MOF-5/GO (0.044 min^{-1}), Ni.S$_2$/MOF-5/GO (0.043 min^{-1}), Mo.S$_2$/MOF-5/GO (0.041 min^{-1}), and Ni/Mo.S$_2$/MOF-5 (0.033 min^{-1}) were calculated from the slope.
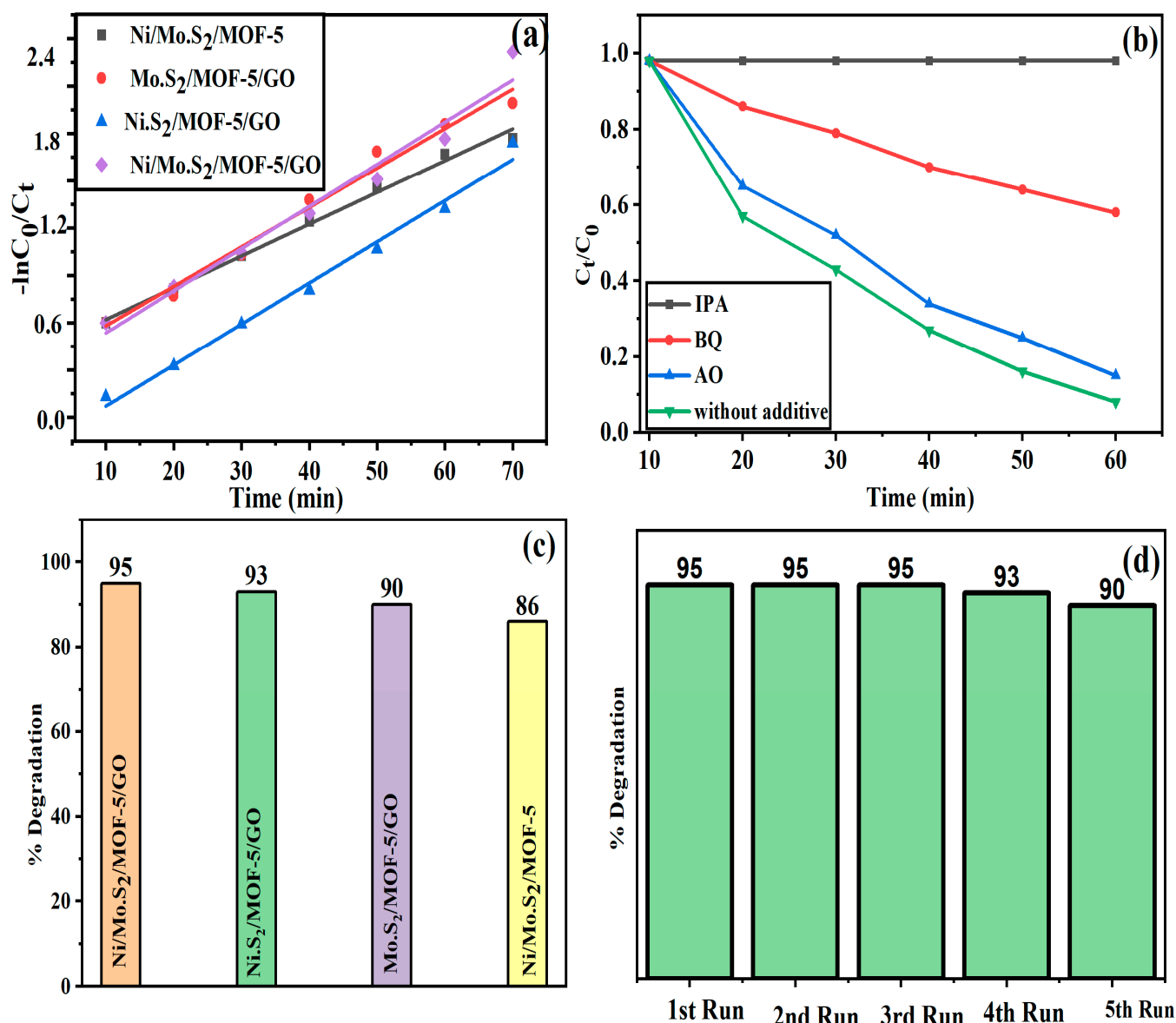
Figure 5. (**a**) Pseudo first-order kinetic model fitting, (**b**) Scavenger test, (**c**) MOX % degradation, and (**d**) Reusability studies for moxifloxacin (MOX) with Ni/Mo.S_2/MOF-5/GO, Ni.S_2/MOF-5/GO, Mo.S_2/MOF-5/GO, and Ni/Mo.S_2/MOF-5 photocatalysts.

The calculated values of k (rate constant) for different photocatalysts used for MOX degradation are presented in Table 2. The rate constant's R^2 values for the synthesized composites were 0.992, 0.981, 0.986 and 0.965, which supported the pseudo-first order kinetics and continuous photodegradation of MOX.

Table 2. Kinetic rate constant (k); Degradation efficiency, percent; and R^2 values of grown nanocomposites.

Sample	Dye	Degradation Efficiency, %	Rate Constant, K (min^{-1})	R^2	Band Gap (±0.1 eV)
Ni/Mo.S_2/MOF-5	MOX	86	0.033	0.992	2.30
Mo.S_2/MOF-5/GO	MOX	90	0.041	0.981	2.27
Ni.S_2/MOF-5/GO	MOX	93	0.043	0.986	2.22
Ni/Mo.S_2/MOF-5/GO	MOX	95	0.044	0.965	2.06

2.7. Detection of the Reactive Species

Designing a potential charge transfer pathway for the degradation of organic pollutants requires careful consideration of the primary reactive species. In order to acquire $(O_2^{\bullet-})$, $(OH^{\bullet})$, and h^+, a number of scavengers: benzoquinone (BQ), isopropyl alcohol (IPA) and ammonium oxalate (AO), respectively, were tested during the degradation of MOX [52,53]. Different scavengers exhibit distinct influences on the photodegradation pathway, as may be seen experimentally. The degradation capacity was significantly decreased when BQ and IPA were introduced to this reaction, as shown in Figure 5b, indicating that photo-generated $(O_2^{\bullet-})$ and $(OH^{\bullet})$ radicals were essential for the degrading process. Moreover, the addition of AO affected the catalyst's ability to degrade, suggesting that the h^+ species were not the main active oxidative species in the photocatalytic degradation of MOX. Furthermore, the significant impact of the presence of $(O_2^{\bullet-})$ on MOX removal was confirmed by BQ addition, and a significant decrease in the MOX photocatalytic ability was observed. However, the remarkable quenching phenomena was seen in the sample with the addition of IPA, showing that the grown $Ni/Mo.S_2/MOF-5/GO$ nanocomposite acts as the top reactive species during MOX removal [54]. The MOX degradation followed the given order of reactive species as $h^+ < O_2^{\bullet-} < OH^{\bullet}$ [55,56], which is well demonstrated in the graphical representation in Figure 5b.

2.8. Effect of Photo-Catalyst on the Photodegradation of MOX

The effect of nanocomposites dosage on MOX degradation with regard to time is depicted in Figure 5c. The order of photodegradation of MOX was followed by all of the synthesized photocatalysts, which are all determined to be active. This demonstrates an increase in degradation efficiency, as the catalyst dose is improved for all $Ni/Mo.S_2/MOF-5/GO$ (95%) > $Ni.S_2/MOF-5/GO$ (93%) > $Mo.S_2/MOF5/GO$ (90%) > $Ni/Mo.S_2/MOF-5$ (86%) up to 2.0 mgL^{-1} (Table 3).

Table 3. Comparison with various studies for degradation of moxifloxacin.

Catalyst	Synthesis Method	Irradiation Time (min)	Light Source	% Degradation	Ref.
Bio-FeMnCoO x	Bio-synthesis	20	---	95.2	[57]
CNABA hybrids	Physico-chemical	50	300 W xenon lamp	65	[58]
Porous sulfurized iron-based composite	Co-precipitation	30	XL (300 W)	97	[59]
$CaBiFe_{85\%}Ti_{15\%}O_3$ Nanoparticle	Co-precipitation	60	UV-visible light	89.16	[60]
$Ni/Mo.S_2/MOF-5/GO$	Solvo-thermal	90	Sunlight (280–320 nm)	95	Current study

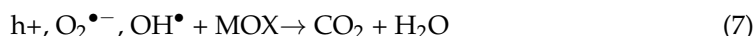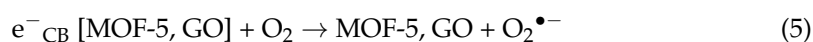*2.9. Stability and Reusability MOF-5/GO Nanocomposites*

As a result of photodegradation, the photocatalyst's activity decreased under continuous exposure. Hence, before using the composites in real applications, it is essential to critically consider their stability and reusability [61]. Figure 5d illustrates the effectiveness of the produced $Ni/Mo.S_2/MOF-5/GO$ nanocatalyst's photocatalytic degradation of MOX over five consecutive cycles. To verify the stability of the used catalysts after cycling, the Fourier transform infrared (FTIR) spectra were taken and no significant change was observed in synthesized nanocomposites, as shown in Figure S3 (Supporting Information).

In the first three cycles it remained constant; however, a minor decline in adsorption percentage was seen in the final two cycles. The MOX molecule may have moved inside the MOF-5/GO nanocomposite's internal cavities, where it could not be readily removed, which may be the reason for the slight decline in the adsorption efficiency of nanocompos-

ites. Nevertheless, faster adsorption, combined with high reversibility as shown by these data, reflects its utility and value for MOX adsorption in practical applications.

2.10. Enhancement Mechanism of Photocatalytic Activity

The enhancement in the photocatalytic mechanism of the $Ni/Mo.S_2/MOF-5/GO$ composite is illustrated in Figure 6, based on the aforementioned experimental results. The results demonstrate that adding $Ni-Mo.S_2$ and GO to the carbon-based/semiconductor/MOF composite improves the photocatalytic activity of MOF-5. Within the MOF-5/GO substrate, $Ni.S_2$ and $Mo.S_2$ clusters may act as quantum fragments, surrounded by terephthalate ligands. When used as antennas, these organic bridging ligands may generate visible light and then efficiently transmit the energy to the $Ni.S_2$ and $Mo.S_2$ clusters. The creation of an (e^-/h^+) pair on the catalyst surface governs the fundamental workings demonstrated in experiments on photocatalytic MOX degradation. Additionally, following GO alteration, the $Ni/Mo.S_2/MOF-5/GO$ composite showed a stronger positive valance band potential, which would increase its capacity for photocatalytic oxidation in the degradation of MOX. The literature states that the Zn-based MOF-5 conduction band potential (E_{CB}) and valence band potential (E_{VB}) are around 1.01 and 2.87 eV vs. NHE, respectively [62]. When MOF-5 gets energized by photons, the electron in the VB state is excited to the CB state. This can be accomplished by making a hole in the VB, causing the photogenerated electrons on the CB MOF-5 to simultaneously move quickly to the GO surface, resulting in effective carrier splitting and increased photocatalytic activity. In this way, the GO sheet will serve as an excellent electron acceptor, and the electron-hole recombination will be interrupted [63,64]. Consequently, because of its two-dimensional pi-conjugate structure, graphene oxide is a great conductor [65]. The electrons on the CB reduce O_2 to generate superoxide radicals $(O_2^{\bullet-})$. However, the standard redox potential of $(H_2O/OH^\bullet)$ = 2.8 eV vs. NHE) was slightly lower than the VB of the catalyst, allowing the holes in the VB of $Ni/Mo.S_2/MOF-5$ to quickly oxidize water to create more $(OH^\bullet)$, increasing the photodegradation efficiency.

$$MOF-5, GO + h\nu \rightarrow e^-_{CB} [MOF-5, GO] + h^+_{VB} [MOF-5, GO] \tag{4}$$

$$e^-_{CB} [MOF-5, GO] + O_2 \rightarrow MOF-5, GO + O_2^{\bullet-} \tag{5}$$

$$h^+_{VB} [MOF-5] + OH^- \rightarrow h^+_{VB}[MOF-5] + OH^\bullet \tag{6}$$

$$h+, O_2^{\bullet-}, OH^\bullet + MOX \rightarrow CO_2 + H_2O \tag{7}$$

As a result of the hydroxyl (OH) group substitution in aqueous solution scavenging the holes in the valance band, an innovative route for the generation of remarkably volatile radicals $(OH^\bullet)$ is created. This $OH^\bullet$ radical dominates the reaction and makes it simpler for reactants to diffuse to the active sites, as the catalyst oxidizes the MOX. The effectiveness of pollutant degradation is dependent on how many active sites are available on the catalyst surface. The hydroxyl, superoxide radicals and holes generated could directly oxidize the MOX molecules to form the degradation by-products CO_2 and H_2O. However, we observed in the radical scavenging experiments that the contribution of the holes and superoxide radicals was less than that of the hydroxyl.
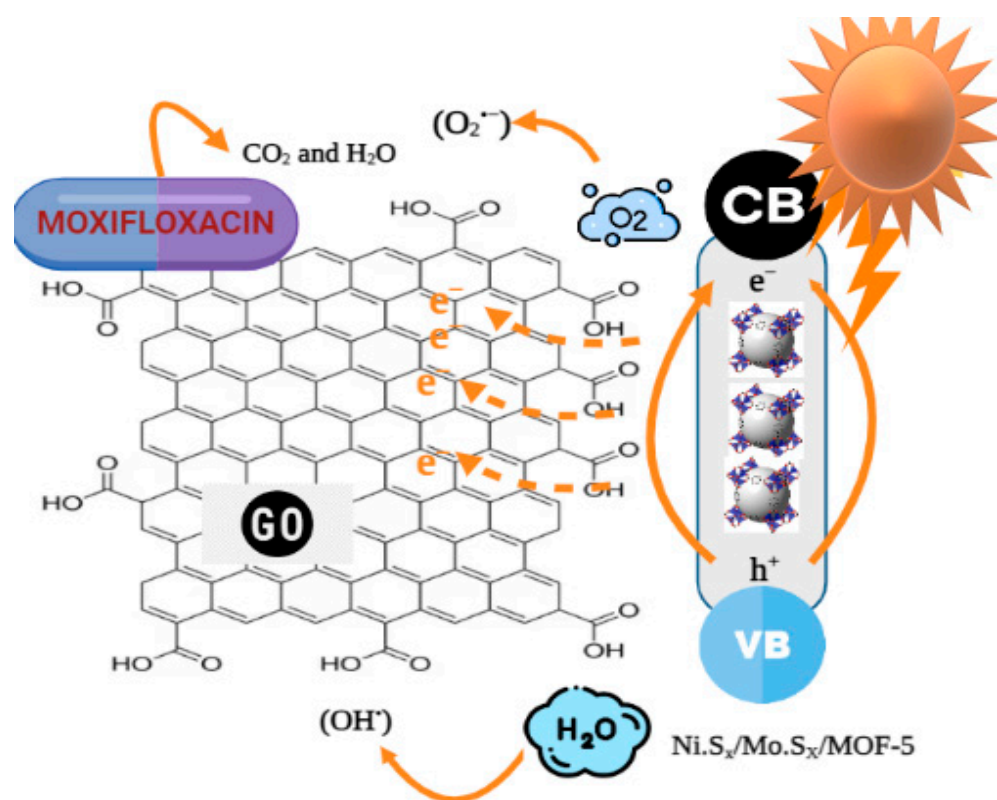
Figure 6. Schematic illustration of the enhanced photocatalytic mechanism of nanocomposite Ni-$Mo.S_2$/MOF-5/GO.

3. Experimental Methods

3.1. Materials

The supplier of the antibiotic moxifloxacin (BAY12-80369 MOX 98%) was Bayer (Berlin, Germany). For our experimental work, natural graphite flakes were purchased from Sigma Aldrich (Saint Louis, United States). Daejung Chemicals (Gyeonggi, Korea) provided the sulfuric acid (H_2SO_4 98.0% purity), anhydrous ethanol (EtOH, 99.8%), potassium permanganate ($KMnO_4$ 99.8%), zinc nitrate hexahydrate [$Zn(NO_3)_2 \cdot 6H_2O$, 99.0%], ethylene glycol (99.9%), and N,N-dimethylformamide (DMF). Without additional purification, terephthalic-acid (1,4-benzenedicarboxylic acid, H_2BDC, 99.9%), hydrochloric-acid (HCl 36%), phosphoric-acid (H_3PO_4 87%) and hydrogen peroxide (H_2O_2 35%) by Duksan Chemical (Ansan, Korea) were all employed as analytical-grade reagents. All studies were conducted using deionized (DI) water.

3.2. Analysis and Characterization

The as-synthesized samples' physicochemical properties were investigated using various tools and methods, such as an X-ray powder diffractometer (XRD)(**9**JDX-3532 JEOL, Tokyo, Japan), An Alpha-Bruker Fourier transform infrared spectroscopy (FTIR(Mannheim, Germany)Scanning electron microscopy (SEM)(JSM5910 JEOL, Tokyo, Japan), and a UV-Vis spectrophotometer(Cecil CE 7400, Waltham, USA). To sonicate the reaction solution, an ultrasonic bath (E30 H Elmasonic) (Elma Ultrasonic, Singen, Germany)was used.

3.3. Zn-Based MOF (MOF-5) Preparation

The DMF technique was used to synthesize the MOF-5, in line with the report, after modification. In a single-step experiment, a homogeneous solution was made by vigorously stirring 0.6 g of $Zn(NO_3)_2 \cdot 6H_2O$ and 0.12 g of terephthalic acid (H_2BDC) with 20 mL of ethylene glycol for an hour. An autoclave composed of stainless steel and coated with Teflon was used to heat the solution for eight hours at 170 °C. The product was obtained by

centrifugation, cooling at room temperature, and repeated washes with DMF and ethanol. The solvent was removed by dissolving the creamy white precipitates in pure chloroform solvent for 24 h at room temperature. The final product was then collected and washed with ethanol before being dried at 70 °C.

3.4. Synthesis of Graphene Oxide (GO)

A modified Hummers method was applied to manufacture GO from graphite powder [66]. A flask equivalent to 50 mL of 98 percent H_2SO_4 was placed in an ice-bath. The flask was then filled with 2.0 g of graphite and vigorously agitated. After that, 6.0 g of $KMnO_4$ was gradually added to the flask while the temperature of the reaction was sustained under 25 °C in an ice bucket for approximately half an hour. The reaction mixture was then heated in a water-bath up to 35 °C, stirred for roughly 45 min, and then added to the flask. The reaction temperature was further raised to 90 °C after adding 50 mL of water to the flask containing the reaction mixture, and the mixture was finally stirred for 30 min.

3.5. Synthesis of Metal Organic Framework-5/Graphene-Oxide (MOF-5/GO)

With multiple changes to a typical MOF-5 [67], the MOF-5/GO nanocomposite was synthesized by adapting the single-step solvothermal method. Initially, 0.6 g of Zn $(NO_3)_2 \cdot 6H_2O$ and 0.12 g of terephthalic acid H_2BDC were dispersed in 60 mL of DMF to obtain a final clean solution. To create a homogenized DMF emulsion of graphene oxide, 0.36 g of GO was sonicated into a solution of 10 mL of DMF for 120 min [68]. Following the addition of the GO suspension, the previously clean solution was stirred for an additional 30 min, before being transferred to a 100 mL stainless-steel autoclave lined with Teflon and heated to 120 °C for 48 h. After that, a vacuum drying process employing a desiccator fitted with a heater at 80 °C for 12 h was used to produce the resulting solid sample, which was cleaned with DMF and $CHCl_3$. The hybrid materials were named MOF-5-GO in their first state of synthesis.

3.6. Fabrication of Ni/MoS$_2$/MOF-5-GO Nanocomposite

A hydrothermal approach was employed to fabricate the MOF-5/GO composite. In 50 mL of deionized water, 0.3 g of sodium molybdate dihydrate ($Na_2MoO_4 \cdot 2H_2O$) and 0.5816 g of nickel nitrate hexahydrate ($Ni(NO_3)_2 \cdot 6H_2O$) were mixed. This mixture was homogenized by using a sonicator for 30 min. Following that, 0.15 g of sodium sulphide nonahydrate was dissolved in 100 mL of DI water to create a 0.006 molar aqueous solution of sodium sulphide nonahydrate ($Na_2S \cdot 9H_2O$); 12 mL of this was pipetted out and added to the above solution. In a further step, 0.25 g of freshly prepared MOF-5/GO was added and it was stirred once more for an hour. The mixture was then transferred to a sealed Teflon vessel and incubated for 21 h at 90 °C. After lowering to room temperature, the catalyst was centrifuged (4500 rpm) for 15 min. The obtained product was a Ni/Mo.S_2/MOF-5/GO composite rinsed with deionized water and anhydrous ethanol. Following that, the precipitates were desiccated for 8 h at 25 °C. The acquired product was finally grounded and stored. By adapting the scheme proposed above in Figure 7a,b the photocatalyst composites Mo.S_2/MOF-5/GO, Ni.S_2/MOF-5/GO, Ni/Mo.S_2/MOF-5 were also successfully synthesized.

3.7. Photocatalytic Experiments

MOF-5-based Ni/Mo.S_2/MOF-5/GO photocatalysts used to degrade moxifloxacin molecules out of wastewater were investigated. In a typical experiment, without adding any further chemicals, the aqueous solution of MOX was created and used as a sample of wastewater. Prior to the desired dilution (10 ppm), the stock solution of MOX (1000 ppm) was prepared by dissolving 0.1 g of MOX in 100 mL of distilled water. In tests involving photocatalytic degradation, 10 mg of photocatalyst was introduced to a photoreactor containing 50 mL of MOX solution atpH 5. The solution was stirred magnetically in a dark room for 30 min, then placed in sunlight for 90 min to observe the adsorption-desorption

equilibrium. Under dark conditions, there was no degradation of MOX observed; however, the photocatalytic efficiency for MOX degradation was significantly enhanced up to 90 min when Ni/Mo.S$_2$/MOF-5/GO composite was irradiated with unfiltered sunlight.
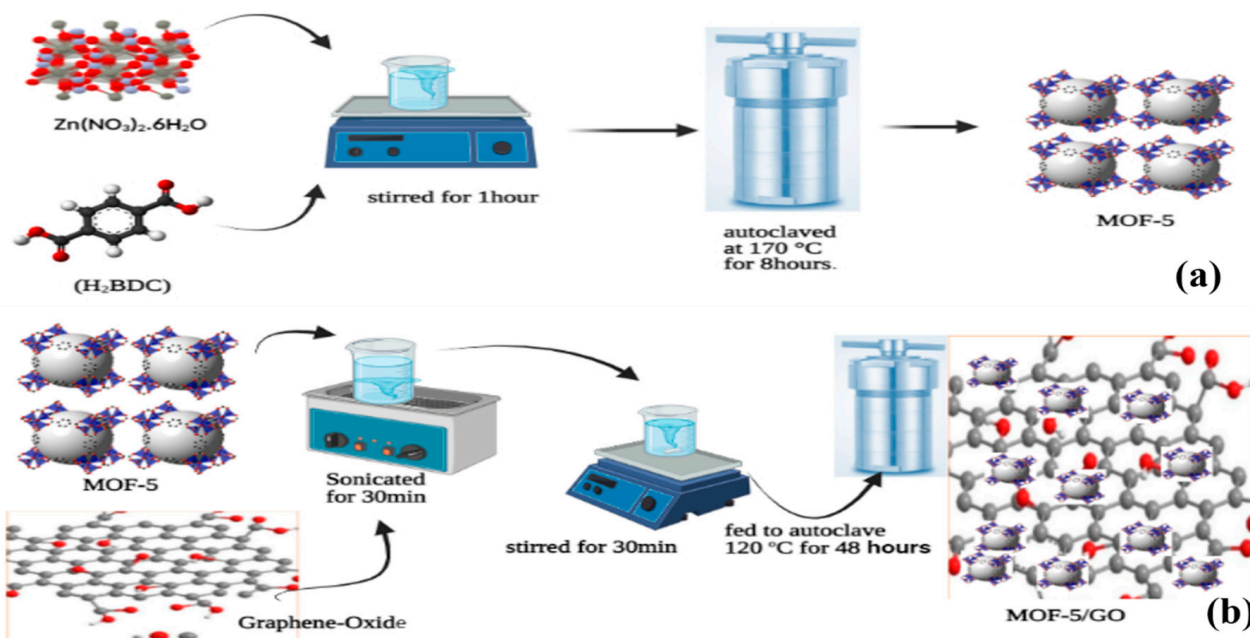
Figure 7. Schematic illustration for the synthesis of (**a**) MOF-5 (**b**) graphene oxide/MOF-5.

During the process, aliquots of 2 mL were withdrawn from the parent solution after 10 min intervals, separated through centrifugation, and the intensity of characteristic electronic absorption band was noted using a UV-Vis spectrophotometer. The degradation of MOX was recorded by observing the reduction in the UV-Vis absorption spectra (max = 290 nm) as a function of exposure time. The following equation was used to calculate MOX (%R) removal efficiency:

$$\% \, R = (C^0 - C)/C^0 \times 100 \tag{8}$$

where, C^0 (mg L^{-1}) is the primary concentration of MOX and C (mg L^{-1}) is the secondary concentration of MOX after photocatalytic decomposition in response to a series of catalysts at different time intervals under UV irradiation [69,70].

4. Conclusions

In summary, we have effectively synthesized a unique hybrid photocatalyst using several bimetallic sulphide combinations and characterized it by XRD, SEM, EDS, FTIR, and UV-Vis analysis. In this article, experimental data confirm that metal organic frameworks with specific surface areas such as MOF-5 can be synthesized by combining double sulfides of bi-metals (nickel and molybdenum). There is a substantial difference in photocatalytic activity between GO modified with sulfides of a single metal (molybdenum or nickel) and GO modified with sulfides of both metals. The hybrid composite Ni/Mo.S$_2$/MOF-5/GO displayed excellent visible light-driven photocatalytic activity in contrast to the other hybrids, Ni.S$_2$/MOF-5/GO, Mo.S$_2$/MOF-5/GO, and Ni-Mo.S$_2$/MOF-5. This was due to the improved photocatalytic performance related to the development of the best junction of the Ni/Mo.S$_2$/MOF-5/GO composite. When photodegradation occurs, GO, with its outstanding conductivity, and MOF, with its specific adsorption action, are both involved. The separation and resettlement of photo-generated carriers benefit from this synergistic action. Consequently, Ni/Mo.S$_2$/MOF-5/GO has good recycling performance, as demonstrated by the cyclic experiment, and its photodegrading efficiency is estimated

to be 95%. The improved photocatalytic activity of the Ni/Mo.S$_2$/MOF-5/GO hybrid was attributable to a significant rise in the overall number of photogenerated electron/hole pairs (e$^-$/h$^+$), and the active species (OH$^\bullet$) and (O$_2{}^{\bullet-}$). Results of scavenger tests confirmed that the OH$^\bullet$ and O$_2{}^{\bullet-}$ radicals were vital to the photodegradation of MOX. The h$^+$ radical, on the other hand, appeared to be a relatively inactive species for degradation. Based on this research, it can be concluded that the modification of the bimetallic sulphide MOF-5 by using GO (electron acceptor) was effective and can serve as an inspiration for the development of other MOF-5/GO composite photocatalysts to increase their applications.

Supplementary Materials: The following supporting information can be downloaded at: https://www.mdpi.com/article/10.3390/catal13060984/s1, Figure S1: Optimization of reaction parameters using Ni/Mo.S$_2$/MOF-5/GO, Ni.S$_2$/MOF-5/GO, Mo.S$_2$/MOF-5/GO, Ni/Mo.S$_2$/MOF-5 (a) MOX concentration, (b) photocatalyst dosage (c) Effect of pH of on degradation of moxifloxacin (d) MOX degradation by all catalysts as a function of time under sunlight irradiation; Figure S2: Fourier transform infrared (FTIR) spectra of sample (a) Ni/Mo.S$_2$/MOF-5/GO, (b) NiS$_2$/MOF-5/GO, (c) Mo.S$_2$/MOF-5/GO, (d)Ni/Mo.S$_2$/MOF-5 nanocomposites of the used catalysts after cycling to verify their structural stability.

References

1. Ji, Y.; Ferronato, C.; Salvador, A.; Yang, X.; Chovelon, J.-M. Degradation of ciprofloxacin and sulfamethoxazole by ferrous-activated persulfate: Implications for remediation of groundwater contaminated by antibiotics. *Sci. Total Environ.* **2014**, *472*, 800–808. [CrossRef]
2. Liu, C.; Mao, S.; Wang, H.; Wu, Y.; Wang, F.; Xia, M.; Chen, Q. Peroxymonosulfate-assisted for facilitating photocatalytic degradation performance of 2D/2D WO$_3$/BiOBr S-scheme heterojunction. *Chem. Eng. J.* **2022**, *430*, 132806. [CrossRef]
3. Liu, C.; Mao, S.; Shi, M.; Wang, F.; Xia, M.; Chen, Q.; Ju, X. Peroxymonosulfate activation through 2D/2D Z-scheme CoAl-LDH/BiOBr photocatalyst under visible light for ciprofloxacin degradation. *J. Hazard. Mater.* **2021**, *420*, 126613. [CrossRef] [PubMed]
4. Oberlé, K.; Capdeville, M.-J.; Berthe, T.; Budzinski, H.; Petit, F. Evidence for a complex relationship between antibiotics and antibiotic-resistant Escherichia coli: From medical center patients to a receiving environment. *Environ. Sci. Technol.* **2012**, *46*, 1859–1868. [CrossRef] [PubMed]
5. Li, M.; Wei, D.; Zhao, H.; Du, Y. Genotoxicity of quinolones: Substituents contribution and transformation products QSAR evaluation using 2D and 3D models. *Chemosphere* **2014**, *95*, 220–226. [CrossRef]
6. Malik, M.; Ibrahim, S.M.; Tahir, A.A.; Nazir, M.A.; Shah, S.S.A.; Wattoo, M.A.; Kousar, R.; Rehman, A.U. Novel approach towards ternary magnetic g-C$_3$N$_4$/ZnO-W/Snx nanocomposite: Photodegradation of nicotine under visible light irradiation. *Int. J. Environ. Anal. Chem.* **2023**, 1–19. [CrossRef]
7. Kumar, O.P.; Shahzad, K.; Nazir, M.A.; Farooq, N.; Malik, M.; Shah, S.S.A.; ur Rehman, A. Photo-Fenton activated C$_3$N$_{4x}$/AgO$_y$@Co$_{1-x}$Bi$_{0.1-y}$O$_7$ dual s-scheme heterojunction towards degradation of organic pollutants. *Opt. Mater.* **2022**, *126*, 112199. [CrossRef]
8. Abbood, N.S.; Ali, N.S.; Khader, E.H.; Majdi, H.S.; Albayati, T.M.; Saady, N.M.C. Photocatalytic degradation of cefotaxime pharmaceutical compounds onto a modified nanocatalyst. *Res. Chem. Intermed.* **2023**, *49*, 43–56. [CrossRef]

9. Kaushal, S.; Kumar, A.; Bains, H.; Singh, P.P. Photocatalytic degradation of tetracycline antibiotic and organic dyes using biogenic synthesized CuO/Fe_2O_3 nanocomposite: Pathways and mechanism insights. *Environ. Sci. Pollut. Res.* **2023**, *30*, 37092–37104. [CrossRef]

10. Jamshaid, M.; Khan, H.; Nazir, M.A.; Wattoo, M.A.; Shahzad, K.; Malik, M.; Rehman, A.-U. A novel bentonite–cobalt doped bismuth ferrite nanoparticles with boosted visible light induced photodegradation of methyl orange: Synthesis, characterization and analysis of physiochemical changes. *Int. J. Environ. Anal. Chem.* **2022**, 1–16. [CrossRef]

11. Li, S.; Wang, C.; Liu, Y.; Liu, Y.; Cai, M.; Zhao, W.; Duan, X. S-scheme MIL-101 (Fe) octahedrons modified Bi_2WO_6 microspheres for photocatalytic decontamination of Cr (VI) and tetracycline hydrochloride: Synergistic insights, reaction pathways, and toxicity analysis. *Chem. Eng. J.* **2023**, *455*, 140943. [CrossRef]

12. Cai, M.; Liu, Y.; Wang, C.; Lin, W.; Li, S. Novel $Cd_{0.5}Zn_{0.5}S/Bi_2MoO_6$ S-scheme heterojunction for boosting the photodegradation of antibiotic enrofloxacin: Degradation pathway, mechanism and toxicity assessment. *Sep. Purif. Technol.* **2023**, *304*, 122401. [CrossRef]

13. Han, Z.; Lv, M.; Shi, X.; Li, G.; Zhao, J.; Zhao, X. Regulating the Electronic Structure of Fe^{3+}-Doped $BiOCl_xI_{1−x}$ Solid Solution by an Amidoxime-Functionalized Fibrous Support for Efficient Photocatalysis. *Adv. Fiber Mater.* **2023**, *5*, 266–281. [CrossRef]

14. Shah, S.S.A.; Jery, A.E.; Najam, T.; Nazir, M.A.; Wei, L.; Hussain, E.; Hussain, S.; Rebah, F.B.; Javed, M.S. Surface engineering of MOF-derived FeCo/NC core-shell nanostructures to enhance alkaline water-splitting. *Int. J. Hydrogen Energy* **2021**, *47*, 5036–5043. [CrossRef]

15. Shah, S.S.A.; Najam, T.; Molochas, C.; Nazir, M.A.; Brouzgou, A.; Javed, M.S.; Rehman, A.U.; Tsiakaras, P. Nanostructure Engineering of Metal–Organic Derived Frameworks: Cobalt Phosphide Embedded in Carbon Nanotubes as an Efficient ORR. *Mol. Catal.* **2021**, *26*, 6672. [CrossRef]

16. Nazir, M.A.; Najam, T.; Zarin, K.; Shahzad, K.; Javed, M.S.; Jamshaid, M.; Bashir, M.A.; Shah, S.S.A.; Rehman, A.U. Enhanced adsorption removal of methyl orange from water by porous bimetallic Ni/Co MOF composite: A systematic study of adsorption kinetics. *Int. J. Environ. Anal. Chem.* **2021**, 1–16. [CrossRef]

17. Nazir, M.A.; Najam, T.; Shahzad, K.; Wattoo, M.A.; Hussain, T.; Tufail, M.K.; Shah, S.S.A.; ur Rehman, A. Heterointerface engineering of water stable ZIF-8@ZIF-67: Adsorption of rhodamine B from water. *Surf. Interfaces* **2022**, *34*, 102324. [CrossRef]

18. Nazir, M.A.; Khan, N.A.; Cheng, C.; Shah, S.S.A.; Najam, T.; Arshad, M.; Sharif, A.; Akhtar, S.; ur Rehman, A. Surface induced growth of ZIF-67 at Co-layered double hydroxide: Removal of methylene blue and methyl orange from water. *Appl. Clay Sci.* **2020**, *190*, 105564. [CrossRef]

19. Kumar, O.P.; Ahmad, M.; Nazir, M.A.; Anum, A.; Jamshaid, M.; Shah, S.S.A.; Rehman, A. Strategic combination of metal–organic frameworks and C_3N_4 for expeditious photocatalytic degradation of dye pollutants. *Environ. Sci. Pollut. Res.* **2022**, *29*, 35300–35313. [CrossRef]

20. Aslam, M.K.; Shah, S.S.A.; Li, S.; Chen, C. Kinetically controlled synthesis of MOF nanostructures: Single-holed hollow core–shell $ZnCoS@Co_9S_8/NC$ for ultra-high performance lithium-ion batteries. *J. Mater. Chem. A* **2018**, *6*, 14083–14090. [CrossRef]

21. Najam, T.; Shah, S.S.A.; Ding, W.; Deng, J.; Wei, Z. Enhancing by nano-engineering: Hierarchical architectures as oxygen reduction/evolution reactions for zinc-air batteries. *J. Power Sources* **2019**, *438*, 226919. [CrossRef]

22. Eddaoudi, M.; Kim, J.; Rosi, N.; Vodak, D.; Wachter, J.; O'Keeffe, M.; Yaghi, O.M. Systematic design of pore size and functionality in isoreticular MOFs and their application in methane storage. *Science* **2002**, *295*, 469–472. [CrossRef]

23. Zhuang, J.-L.; Terfort, A.; Wöll, C. Formation of oriented and patterned films of metal–organic frameworks by liquid phase epitaxy: A review. *Coord. Chem. Rev.* **2016**, *307*, 391–424. [CrossRef]

24. Behera, P.; Subudhi, S.; Tripathy, S.P.; Parida, K. MOF derived nano-materials: A recent progress in strategic fabrication, characterization and mechanistic insight towards divergent photocatalytic applications. *Coord. Chem. Rev.* **2022**, *456*, 214392. [CrossRef]

25. Juan-Alcaniz, J.; Gielisse, R.; Lago, A.B.; Ramos-Fernandez, E.V.; Serra-Crespo, P.; Devic, T.; Guillou, N.; Serre, C.; Kapteijn, F.; Gascon, J. Towards acid MOFs–catalytic performance of sulfonic acid functionalized architectures. *Catal. Sci. Technol.* **2013**, *3*, 2311–2318. [CrossRef]

26. Abdelhamid, H.N.; Mathew, A.P. Cellulose–metal organic frameworks (CelloMOFs) hybrid materials and their multifaceted Applications: A review. *Coord. Chem. Rev.* **2022**, *451*, 214263. [CrossRef]

27. Geim, A.K.; Novoselov, K.S. The rise of graphene. *Nat. Mater.* **2007**, *6*, 183–191. [CrossRef]

28. Farooq, N.; Luque, R.; Hessien, M.M.; Qureshi, A.M.; Sahiba, F.; Nazir, M.A.; ur Rehman, A. A Comparative Study of Cerium- and Ytterbium-Based $GO/g-C_3N_4/Fe_2O_3$ Composites for Electrochemical and Photocatalytic Applications. *Appl. Sci.* **2021**, *11*, 9000. [CrossRef]

29. Jahan, M.; Bao, Q.; Yang, J.-X.; Loh, K.P. Structure-directing role of graphene in the synthesis of metal− organic framework nanowire. *J. Am. Chem. Soc.* **2010**, *132*, 14487–14495. [CrossRef]

30. Petit, C.; Bandosz, T.J. MOF–graphite oxide composites: Combining the uniqueness of graphene layers and metal–organic frameworks. *Adv. Mater.* **2009**, *21*, 4753–4757. [CrossRef]

31. Yang, Z.; Xu, X.; Liang, X.; Lei, C.; Gao, L.; Hao, R.; Lu, D.; Lei, Z. Fabrication of Ce doped UiO-66/graphene nanocomposites with enhanced visible light driven photoactivity for reduction of nitroaromatic compounds. *Appl. Surf. Sci.* **2017**, *420*, 276–285. [CrossRef]

32. Vickers, N.J. Animal communication: When i'm calling you, will you answer too? *Curr. Biol.* **2017**, *27*, R713–R715. [CrossRef] [PubMed]

33. Ramli, Z.; Kamarudin, S. Platinum-based catalysts on various carbon supports and conducting polymers for direct methanol fuel cell applications: A review. *Nanoscale Res. Lett.* **2018**, *13*, 410. [CrossRef] [PubMed]

34. Kaushal, S.; Kumari, V.; Singh, P.P. Sunlight-driven photocatalytic degradation of ciprofloxacin and organic dyes by biosynthesized rGO–ZrO$_2$ nanocomposites. *Environ. Sci. Pollut. Res.* **2023**, *30*, 65602–65617. [CrossRef]

35. Huang, L.; Wang, H.; Chen, J.; Wang, Z.; Sun, J.; Zhao, D.; Yan, Y. Synthesis, morphology control, and properties of porous metal–organic coordination polymers. *Microporous Mesoporous Mater.* **2003**, *58*, 105–114. [CrossRef]

36. Bonino, F.; Chavan, S.; Vitillo, J.G.; Groppo, E.; Agostini, G.; Lamberti, C.; Dietzel, P.D.; Prestipino, C.; Bordiga, S. Local structure of CPO-27-Ni metallorganic framework upon dehydration and coordination of NO. *Chem. Mater.* **2008**, *20*, 4957–4968. [CrossRef]

37. Divya, K.; Chandran, A.; Reethu, V.; Mathew, S. Enhanced photocatalytic performance of RGO/Ag nanocomposites produced via a facile microwave irradiation for the degradation of Rhodamine B in aqueous solution. *Appl. Surf. Sci.* **2018**, *444*, 811–818. [CrossRef]

38. Karimzadeh, Z.; Javanbakht, S.; Namazi, H. Carboxymethylcellulose/MOF-5/Graphene oxide bio-nanocomposite as antibacterial drug nanocarrier agent. *BioImpacts* **2019**, *9*, 5. [CrossRef]

39. Jabbari, V.; Veleta, J.; Zarei-Chaleshtori, M.; Gardea-Torresdey, J.; Villagrán, D. Green synthesis of magnetic MOF@ GO and MOF@ CNT hybrid nanocomposites with high adsorption capacity towards organic pollutants. *Chem. Eng. J.* **2016**, *304*, 774–783. [CrossRef]

40. Liu, L.; Zhang, B.; Zhang, Y.; He, Y.; Huang, L.; Tan, S.; Cai, X. Simultaneous removal of cationic and anionic dyes from environmental water using montmorillonite-pillared graphene oxide. *J. Chem. Eng. Data* **2015**, *60*, 1270–1278. [CrossRef]

41. Bahuguna, A.; Choudhary, P.; Chhabra, T.; Krishnan, V. Ammonia-doped polyaniline–graphitic carbon nitride nanocomposite as a heterogeneous green catalyst for synthesis of indole-substituted 4 H-chromenes. *ACS Omega* **2018**, *3*, 12163–12178. [CrossRef]

42. Tran, N.T.; Kim, D.; Yoo, K.S.; Kim, J. Synthesis of Cu-doped MOF-235 for the Degradation of Methylene Blue under Visible Light Irradiation. *Bull. Korean Chem. Soc.* **2019**, *40*, 112–117. [CrossRef]

43. Malik, M.; Ibrahim, S.M.; Nazir, M.A.; Tahir, A.A.; Tufail, M.K.; Shah, S.S.A.; Anum, A.; Wattoo, M.A.; Rehman, A.u. Engineering of a Hybrid g-C$_3$N$_4$/ZnO-W/Co$_x$ Heterojunction Photocatalyst for the Removal of Methylene Blue Dye. *Catalysts* **2023**, *13*, 813. [CrossRef]

44. Moniz, S.J.; Shevlin, S.A.; Martin, D.J.; Guo, Z.-X.; Tang, J. Visible-light driven heterojunction photocatalysts for water splitting–a critical review. *Energy Environ. Sci.* **2015**, *8*, 731–759. [CrossRef]

45. Bandosz, T.J.; Petit, C. MOF/graphite oxide hybrid materials: Exploring the new concept of adsorbents and catalysts. *Adsorption* **2011**, *17*, 5–16. [CrossRef]

46. Mohammadi, A.A.; Moghanlo, S.; Kazemi, M.S.; Nazari, S.; Ghadiri, S.K.; Saleh, H.N.; Sillanpää, M. Comparative removal of hazardous cationic dyes by MOF-5 and modified graphene oxide. *Sci. Rep.* **2022**, *12*, 15314. [CrossRef]

47. Thi, Q.V.; Tamboli, M.S.; Ta, Q.T.H.; Kolekar, G.B.; Sohn, D. A nanostructured MOF/reduced graphene oxide hybrid for enhanced photocatalytic efficiency under solar light. *Mater. Sci. Eng. B* **2020**, *261*, 114678. [CrossRef]

48. Mazlan, N.A.; Butt, F.S.; Lewis, A.; Yang, Y.; Yang, S.; Huang, Y. The Growth of Metal–Organic Frameworks in the Presence of Graphene Oxide: A Mini Review. *Membranes* **2022**, *12*, 501. [CrossRef]

49. Chen, Y.; Zhai, B.; Liang, Y. Enhanced degradation performance of organic dyes removal by semiconductor/MOF/graphene oxide composites under visible light irradiation. *Diam. Relat. Mater.* **2019**, *98*, 107508. [CrossRef]

50. Petit, C.; Bandosz, T.J. Exploring the coordination chemistry of MOF–graphite oxide composites and their applications as adsorbents. *Dalton Trans.* **2012**, *41*, 4027–4035. [CrossRef]

51. Yang, C.; You, X.; Cheng, J.; Zheng, H.; Chen, Y. A novel visible-light-driven In-based MOF/graphene oxide composite photocatalyst with enhanced photocatalytic activity toward the degradation of amoxicillin. *Appl. Catal. B Environ.* **2017**, *200*, 673–680. [CrossRef]

52. Saravanakumar, K.; Muthuraj, V.; Jeyaraj, M. The design of novel visible light driven Ag/CdO as smart nanocomposite for photodegradation of different dye contaminants. *Spectrochim. Acta Part A Mol. Biomol. Spectrosc.* **2018**, *188*, 291–300. [CrossRef] [PubMed]

53. Dhanalakshmi, M.; Saravanakumar, K.; Prabavathi, S.L.; Abinaya, M.; Muthuraj, V. Fabrication of novel surface plasmon resonance induced visible light driven iridium decorated SnO$_2$ nanorods for degradation of organic contaminants. *J. Alloys Compd.* **2018**, *763*, 512–524. [CrossRef]

54. Van Doorslaer, X.; Heynderickx, P.M.; Demeestere, K.; Debevere, K.; Van Langenhove, H.; Dewulf, J. TiO$_2$ mediated heterogeneous photocatalytic degradation of moxifloxacin: Operational variables and scavenger study. *Appl. Catal. B Environ.* **2012**, *111*, 150–156. [CrossRef]

55. Prabavathi, S.L.; Saravanakumar, K.; Nkambule, T.; Muthuraj, V.; Mamba, G. Enhanced photoactivity of cerium tungstate-modified graphitic carbon nitride heterojunction photocatalyst for the photodegradation of moxifloxacin. *J. Mater. Sci. Mater. Electron.* **2020**, *31*, 11434–11447. [CrossRef]

56. Chen, Y.; Zhai, B.; Liang, Y.; Li, Y. Hybrid photocatalysts using semiconductor/MOF/graphene oxide for superior photodegradation of organic pollutants under visible light. *Mater. Sci. Semicond. Process.* **2020**, *107*, 104838. [CrossRef]

57. Xu, A.; Wu, D.; Zhang, R.; Fan, S.; Lebedev, A.T.; Zhang, Y. Bio-synthesis of Co-doped FeMnO$_x$ and its efficient activation of peroxymonosulfate for the degradation of moxifloxacin. *Chem. Eng. J.* **2022**, *435*, 134695. [CrossRef]

58. Liu, Y.; Bian, C.; Li, Y.; Sun, P.; Xiao, Y.; Xiao, X.; Wang, W.; Dong, X. Aminobenzaldehyde convelently modified graphitic carbon nitride photocatalyst through Schiff base reaction: Regulating electronic structure and improving visible-light-driven photocatalytic activity for moxifloxacin degradation. *J. Colloid Interface Sci.* **2023**, *630*, 867–878. [CrossRef] [PubMed]

59. Zhang, X.; Kang, X.; Wu, J.; Yang, Q.; Zhang, Y.; He, J.; Zheng, C.; Yang, Y.; Ye, Z. Sulfur-doped mesoporous ferric oxide used for effectively activating H$_2$O$_2$ to degrade moxifloxacin. *J. Environ. Chem. Eng.* **2023**, *11*, 109526. [CrossRef]

60. Jamshaid, M.; Khan, M.I.; Fernandez, J.; Shanableh, A.; Hussain, T.; ur Rehman, A. Synthesis of Ti^{4+} doped Ca-BiFO$_3$ for the enhanced photodegradation of moxifloxacin. *New J. Chem.* **2022**, *46*, 19848–19856. [CrossRef]

61. Motlagh, P.Y.; Khataee, A.; Rad, T.S.; Hassani, A.; Joo, S.W. Fabrication of ZnFe-layered double hydroxides with graphene oxide for efficient visible light photocatalytic performance. *J. Taiwan Inst. Chem. Eng.* **2019**, *101*, 186–203. [CrossRef]

62. Yao, T.; Tan, Y.; Zhou, Y.; Chen, Y.; Xiang, M. Preparation of core-shell MOF-5/Bi$_2$WO$_6$ composite for the enhanced photocatalytic degradation of pollutants. *J. Solid State Chem.* **2022**, *308*, 122882. [CrossRef]

63. Dreyer, D.R.; Jia, H.-P.; Todd, A.D.; Geng, J.; Bielawski, C.W. Graphite oxide: A selective and highly efficient oxidant of thiols and sulfides. *Org. Biomol. Chem.* **2011**, *9*, 7292–7295. [CrossRef] [PubMed]

64. Govindaraju, S.; Arumugasamy, S.K.; Chellasamy, G.; Yun, K. Zn-MOF decorated bio activated carbon for photocatalytic degradation, oxygen evolution and reduction catalysis. *J. Hazard. Mater.* **2022**, *421*, 126720. [CrossRef]

65. Som, T.; Troppenz, G.V.; Wendt, R.; Wollgarten, M.; Rappich, J.; Emmerling, F.; Rademann, K. Graphene Oxide/α-Bi$_2$O$_3$ Composites for Visible-Light Photocatalysis, Chemical Catalysis, and Solar Energy Conversion. *ChemSusChem* **2014**, *7*, 854–865. [CrossRef] [PubMed]

66. Khan, N.A.; Shaheen, S.; Najam, T.; Shah, S.S.A.; Javed, M.S.; Nazir, M.A.; Hussain, E.; Shaheen, A.; Hussain, S.; Ashfaq, M. Efficient removal of norfloxacin by MOF@GO composite: Isothermal, kinetic, statistical, and mechanistic study. *Toxin Rev.* **2021**, *40*, 915–927. [CrossRef]

67. Hafizovic, J.; Bjørgen, M.; Olsbye, U.; Dietzel, P.D.; Bordiga, S.; Prestipino, C.; Lamberti, C.; Lillerud, K.P. The inconsistency in adsorption properties and powder XRD data of MOF-5 is rationalized by framework interpenetration and the presence of organic and inorganic species in the nanocavities. *J. Am. Chem. Soc.* **2007**, *129*, 3612–3620. [CrossRef] [PubMed]

68. Huang, Z.-H.; Liu, G.; Kang, F. Glucose-promoted Zn-based metal–organic framework/graphene oxide composites for hydrogen sulfide removal. *ACS Appl. Mater. Interfaces* **2012**, *4*, 4942–4947. [CrossRef]

69. Munawar, T.; Yasmeen, S.; Hussain, F.; Mahmood, K.; Hussain, A.; Asghar, M.; Iqbal, F. Synthesis of novel heterostructured ZnO-CdO-CuO nanocomposite: Characterization and enhanced sunlight driven photocatalytic activity. *Mater. Chem. Phys.* **2020**, *249*, 122983. [CrossRef]

70. Ali, N.S.; Jabbar, N.M.; Alardhi, S.M.; Majdi, H.S.; Albayati, T.M. Adsorption of methyl violet dye onto a prepared bio-adsorbent from date seeds: Isotherm, kinetics, and thermodynamic studies. *Heliyon* **2022**, *8*, e10276. [CrossRef]